Disk collapse in general relativity

Andrew M. Abrahams,* Stuart L. Shapiro,† and Saul A. Teukolsky‡
Center for Radiophysics and Space Research, Cornell University, Ithaca, New York 14853
(Received 25 May 1994)

The radial collapse of a homogeneous disk of collisionless particles can be solved analytically in Newtonian gravitation. To solve the problem in general relativity, however, requires the full machinery of numerical relativity. The collapse of a disk is the simplest problem that exhibits the two most significant and challenging features of strong-field gravitation: black hole formation and gravitational wave generation. We carry out dynamical calculations of several different relativistic disk systems. We explore the growth of ring instabilities in equilibrium disks, and how they are suppressed by sufficient velocity dispersion. We calculate waveforms from oscillating disks, and from disks that undergo gravitational collapse to black holes. Studies of disk collapse to black holes should also be useful for developing new techniques for numerical relativity, such as apparent horizon boundary conditions for black hole spacetimes.

PACS number(s): 04.25.Dm, 04.20.Jb, 04.30.Db, 04.70.−s

I. INTRODUCTION

The simplest example of gravitational collapse is that of a homogeneous sphere of particles initially at rest. This collapse solution is analytic both in Newtonian gravity and general relativity. In general relativity, this solution is known as Oppenheimer-Snyder collapse [1] (the solution is a "piece" of a closed Friedmann universe). Because of Birkhoff's theorem we know that this solution is nonradiating. Both the particle motion and the gravitational field are radially symmetric, i.e., functions of one spatial variable.

The radiating problem which is the simplest analogue to Oppenheimer-Snyder collapse is that of an axisymmetric, infinitely thin disk of particles initially at rest. This case is simple because the particle motion still depends on only one spatial coordinate, although the gravitational field now depends on two. If the disk is constructed by squashing a homogeneous sphere into a pancake, keeping the density homogeneous, then the solution is still analytic in Newtonian theory [2].

However, to solve the problem for relativistic gravitation requires the full machinery of numerical relativity, and has not been addressed until now. Indeed, the dynamical properties of a disk of collisionless particles has never been studied in general relativity, although it has been extensively treated in Newtonian theory [3]. In this paper we tackle the collapse of an axisymmetric collisionless disk of particles in general relativity theory. Particles in an axisymmetric disk can also have angular motion, but because of conservation of angular momentum this motion is not dynamical. We consider cases in which the disk particles are initially at rest and also in which they have initial angular motion. In the latter case we focus on disks with total $J = 0$, i.e., with equal numbers of corotating and counterrotating particles.

In Newtonian theory, it is known that equilibrium disks supported against collapse by rotation alone are unstable to ring formation [3]. The disk can be stabilized by "heating" the disk, that is, converting some of the ordered rotational energy into random "thermal" motion [4]. We explore here whether or not a similar result holds in general relativity.

Our study of disks is geared to analyze two relativistic phenomena that do not arise in Newtonian theory: collapse to black holes and the generation of gravitational waves. Since this is the simplest wave generation problem, disk collapse provides a useful proving ground for testing codes designed to treat gravitational radiation in general relativity. Once we can evolve disk systems accurately in general relativity, we should be able to compute the gravitational field from any axisymmetric source, since the equations for the field are essentially the same as those for general axisymmetric sources. The major problems associated with general axisymmetric collapse are all contained in this test case: formation and evolution of black holes and propagation of gravitational waves.

We have previously studied disk collapse in the context of nonlinear scalar gravitation, where many of the techniques for handling infinitely thin disks were developed [2]. The basic code for evolving axisymmetric spacetimes in general relativity has been discussed in a number of papers [5–7]. We will refer extensively to the equations in Ref. [6] in the discussion that follows. The organization of this paper is as follows. In Sec. II we present the equations for an evolving, general relativistic disk. In Sec. III we discuss analytic test problems including Newtonian and relativistic disk solutions. In Sec. IV we give the results of our numerical calculations.

*Also at the Laboratory of Nuclear Studies, Cornell University, Ithaca, NY 14853. Current address: Department of Physics and Astronomy, University of North Carolina, Chapel Hill, NC 27599.
†Also at the Departments of Astronomy and Physics, Cornell University, Ithaca, NY 14853.
‡Also at the Departments of Physics and Astronomy, Cornell University, Ithaca, NY 14853.

II. BASIC EQUATIONS

The particles comprising the disk are assumed to interact exclusively by gravitation; i.e., they obey the relativistic collisionless Boltzmann equation (Vlasov equation). Accordingly, we have constructed a numerical code that solves Einstein's equations for the gravitational field coupled to matter sources obeying the Vlasov equation. This is the same mean-field, particle simulation code described in Refs. [5,6] to study nonspherical gravitational collapse. The code is designed to handle axisymmetric systems with no net angular momentum. The present version assumes equatorial symmetry. We solve the field equations in 3 + 1 form following Arnowitt, Deser, and Misner [8]. We use maximal time slicing and quasi-isotropic spatial gauge in axisymmetry. The metric, written in spherical-polar coordinates is

$$ds^2 = -\alpha^2 dt^2 + A^2(dr + \beta^r dt)^2 + A^2 r^2(d\theta + \beta^\theta dt)^2 + B^2 r^2 \sin^2\theta d\phi^2. \quad (1)$$

The matter satisfies the relativistic Vlasov equation, which we solve by particle simulation in the mean gravitational field. The basic code is identical to the one described in Refs. [5]. The key equations and definitions of variables are given in the Appendix of Ref. [6]. The equations below are written in terms of the auxiliary variables $\psi = B^{1/2}$, $T = A/B$, and $\eta = \ln T$. (These were generalized to include net rotation in Ref. [7].)

A. Jump conditions

The disk matter source affects the metric via jump conditions in the field equations across the equatorial (disk) plane. These jump conditions replace the usual matter source terms that appear in the field equations. A derivation and numerical implementation of such a jump condition was presented in Ref. [2] for the simple case of scalar gravity. There the governing equation is a nonlinear wave equation with a matter source on the right-hand side.

As an example of how the jump conditions may be derived in 3 + 1 general relativity, consider the two momentum constraint equations (A4) and (A5) in Ref. [6]:

$$\frac{1}{\sin\theta}\partial_\theta(\sin\theta\ \hat{K}^r{}_r) + \frac{T}{\sin^2\theta}\partial_\theta\left(\frac{\sin^2\theta}{T}\hat{K}^\phi{}_\phi\right) = -S_\theta + \frac{1}{r^2}\partial_r(r^2\hat{K}^r{}_\theta), \quad (2)$$

$$\frac{1}{r^3}\partial_r(r^3\hat{K}^r{}_r) + \hat{K}^\phi{}_\phi\,\partial_r\eta = S_r - \frac{1}{r^2\sin\theta}\partial_\theta(\sin\theta\ \hat{K}^r{}_\theta). \quad (3)$$

Since the particles are confined to the equatorial plane $\theta = \pi/2$ where $\beta^\theta = 0$, the particle four-velocity component satisfies $u^\theta = u_\theta = 0$. Hence $S_\theta = 0$. Equation (2) integrated across the equator yields

$$\int_-^+ r\sin\theta d\theta\left[\frac{1}{\sin\theta}\partial_\theta(\sin\theta\ \hat{K}^r{}_r) + \frac{T}{\sin^2\theta}\partial_\theta\left(\frac{\sin^2\theta}{T}\hat{K}^\phi{}_\phi\right) = -S_\theta + \frac{1}{r^2}\partial_r(r^2\hat{K}^r{}_\theta)\right], \quad (4)$$

where $\pm$ denotes $\theta = \pi/2 \pm \epsilon$, $\epsilon \to 0$. Functions that are symmetric across the equatorial plane, such as $\hat{K}^r_r$ and $\hat{K}^\phi_\phi$, are continuous there. Hence Eq. (4) reduces to $0 = 0$. Now consider Eq. (3). Integrating it gives

$$0 = \int_-^+ S_r r\sin\theta d\theta - \frac{1}{r}\hat{K}^r_\theta|^+_-. \quad (5)$$

Since $\hat{K}^r_\theta$ is antisymmetric across the equator, Eq. (5) gives

$$\hat{K}^r_\theta|^+ = -\hat{K}^r_\theta|^- = \frac{r}{2}\int_-^+ S_r r\sin\theta d\theta. \quad (6)$$

Similarly, integration of the Hamiltonian constraint equation [Eq. (A6) of Ref. [6]] leads to

$$\frac{1}{r}\sin\theta\psi_{,\theta}|^+ = -\frac{1}{4r}\psi\eta_{,\theta} - \frac{1}{8\psi}\int_-^+ \rho^* r\sin\theta d\theta. \quad (7)$$

Integrating the lapse equation [Ref. [6], Eq. (A7)] gives

$$\frac{1}{r}\sin\theta(\alpha\psi)_{,\theta}|^+ = -\frac{1}{4r}\alpha\psi\eta_{,\theta}|^+ + \frac{1}{8}\frac{\alpha\psi}{B}\int_-^+ (\rho^* + 2S)r\sin\theta d\theta. \quad (8)$$

The boundary condition Eq. (6) is used to set the value of $\hat{K}^r_\theta$ all along the equatorial plane. In the vacuum, outside of the equatorial plane, $\hat{K}^r_\theta$ is determined by integrating the evolution equation, Eq. (A3) of Ref. [6], as usual.

When finite differencing the Hamiltonian constraint [Eq. (A6) of Ref. [6]], the derivative terms $\psi_{,\theta}$ and $\eta_{,\theta}$ appear in exactly the combination as in Eq. (7). The only place where the matter source term ρ^* appears in the Hamiltonian constraint is through this boundary condition. Equation (8) is used in an analogous fashion for the lapse equation [Ref. [6], Eq. (A7)].

The dynamical equation for η [Ref. [6] Eq. (A2)] and the shift equations [Ref. [6], Eqs. (A8) and (A9)] for β^r and β^ϕ remain unchanged. Note that η, β^r, and β^ϕ are metric coefficients and thus must be continuous across the equator.

B. Matter sources

The geodesic equations of motion for the collisionless matter particles are given by Eqs. (A10)–(A16) of Ref. [6] with the following simplifications: $u_\theta = 0$ and $\theta = \pi/2$.

Hence, as in spherical symmetry, only the radial motion is dynamical for an infinitely thin disk.

The particles are binned in annuli to determine the source terms for the field equations. Equations (A17)–(A21) of Ref. [6] lead to the disk sources [9]

$$\sigma \equiv \int_{-}^{+} \rho^* r \sin\theta d\theta = \sum_j \frac{m\hat{u}_j}{(2\pi r \Delta r)_j}, \tag{9}$$

$$\Sigma_r \equiv \int_{-}^{+} S_r r \sin\theta d\theta = \sum_j \frac{m(u_r)_j}{(2\pi r \Delta r)_j}, \tag{10}$$

$$\Sigma \equiv \int_{-}^{+} S r \sin\theta d\theta = \int_{-}^{+} \rho^* r \sin\theta d\theta - \sum_j \frac{m}{\hat{u}_j (2\pi r \Delta r)_j}. \tag{11}$$

Here m is the particle rest mass related to the total rest mass M_0 by $m = M_0/N$ with N the total particle number. We obtain M_0 from

$$M_0 = \int \sigma_0 2\pi r dr, \tag{12}$$

where

$$\sigma_0 \equiv \int_{-}^{+} \rho_0 r \sin\theta d\theta = \sum_j \frac{m}{(2\pi r \Delta r)_j}, \tag{13}$$

and where ρ_0 is the rest-mass density.

C. Hydrodynamical disks

In the special case in which concentric shells of particles do not cross, collisionless matter may be treated as hydrodynamical dust. Thus, as an alternative to integrating geodesic equations followed by binning of particles, one could integrate the equations of relativistic hydrodynamics. The hydrodynamical equations have the disadvantage that they are partial differential equations (PDE's) and not ordinary differential equations (ODE's) such as the geodesic equations. However, they have the advantage that they produce intrinsically smooth source profiles, unlike particle descriptions which are stochastic.

The basic equations of relativistic hydrodynamics in 3+1 Arnowitt-Deser-Misner (ADM) form are given in, e.g., Ref. [10]. For a cold axisymmetric disk they reduce to the continuity and radial Euler equations:

$$\partial_t \sigma_0 + \frac{1}{r}\partial_r (r \sigma_0 v^r) = 0, \tag{14}$$

$$\partial_t \Sigma_r + \frac{1}{r}\partial_r (r \Sigma_r v^r) = -\sigma \partial_r \alpha + \Sigma_r \partial_r \beta^r + \Sigma \partial_r \ln A\alpha, \tag{15}$$

where

$$\sigma = \left(\sigma_0^2 + \frac{\Sigma_r^2}{A^2}\right)^{1/2}, \tag{16}$$

$$v^r = \frac{\alpha}{A^2}\frac{\Sigma_r}{\sigma} - \beta^r, \tag{17}$$

$$\Sigma = \frac{\Sigma_r^2}{\sigma A^2}. \tag{18}$$

III. ANALYTIC SOLUTIONS AND TESTS

Before we consider numerical solutions of the dynamical equations for disks and their gravitational fields, we give here some analytic results that will serve as code checks and initial data for our evolutions.

A. Oscillating Newtonian disks

As discussed in Ref. [2], there exists a complete analytic solution that furnishes a good test of a numerical disk code in the weak-field, slow-motion limit. The solution describes an oscillating homogeneous spheroid in Newtonian gravitation in the disk limit (eccentricity $e \to 1$). The surface density of such a disk of mass M and radius R is

$$\sigma(r) = \frac{3M}{2\pi R^2}\left(1 - \frac{r^2}{R^2}\right)^{1/2}. \tag{19}$$

Start with the equation of motion for the semimajor axis R of an oblate homogeneous spheroid [e.g., Eq. (5.6) of Ref. [11]]. Take the limit $e \to 1$ and find

$$\ddot{R} = -\frac{3\pi}{4}\frac{GM}{R^2} + \frac{h^2}{R^3}, \tag{20}$$

where h is the conserved angular momentum per unit mass of a particle at the surface. Since the motion is homologous, the radius of each particle satisfies a similar equation. Choose h to be a fraction ξ of the equilibrium angular momentum $h_0 = (3\pi G M R_0/4)^{1/2}$. Set

$$R = R_0 X(t). \tag{21}$$

Then the radius r of each particle satisfies

$$r = r_0 X(t), \tag{22}$$

where r_0 is the initial radius. Substituting Eq. (21) into Eq. (20) we see that X satisfies the familiar equation of an elliptic orbit for a particle with specific angular momentum $h_{\rm eff} = \xi(M/R_0^3)^{1/2}$ around a fixed central mass $M_{\rm eff} = 3\pi M/4$. The parametric solution for $X(t)$ is

$$X = a(1 - e\cos u), \tag{23}$$

$$t = \frac{P}{2\pi}(u - e\sin u) - \frac{P}{2}, \tag{24}$$

where we assume $X = 1$ and $\dot{X} = 0$ at $t = 0$. In Eqs. (23) and (24), the semimajor axis, eccentricity, and period are given by

$$a = \frac{1}{2 - \xi^2},$$
$$e = 1 - \xi^2,$$
$$P = 2\pi\left(\frac{4R_0^3}{3\pi G M (2-\xi^2)^3}\right)^{1/2}. \tag{25}$$

The radial and tangential particle velocities are given by

$$v_r = \frac{\dot{X}}{X} r, \tag{26}$$

$$v_\phi = \xi \frac{r}{X^2} \left(\frac{3\pi GM}{4R_0^3} \right)^{1/2}. \tag{27}$$

It is simple to derive the gravitational wave amplitude for an oscillating disk in the quadrupole approximation. In axisymmetry, in the absence of rotation, there is only one polarization and its amplitude is given by

$$rh_+ = \frac{3}{2} \ddot{I}_{zz} \sin^2 \theta, \tag{28}$$

where

$$I_{zz} = -\frac{1}{3} \int r^2 \rho d^3x = -\frac{2\pi}{3} \int r^3 \sigma dr = -\frac{2}{15} MR^2. \tag{29}$$

Here we have used Eq. (19). Using Eqs. (20) and (21) we find

$$rh_+ = -\frac{2}{5} M \sin^2 \theta \left[R_0^2 \dot{X}^2 + \frac{3\pi M}{4R_0} \left(-\frac{1}{X} + \frac{\xi^2}{X^2} \right) \right]_{t-r}. \tag{30}$$

B. Kalnajs disk

When $\xi = 1$, the above Newtonian disk solution corresponds to a uniformly rotating disk in dynamical equilibrium. As mentioned in the Introduction, such a disk is unstable to the formation of rings but can be stabilized by heating. Kalnajs [4] has given an analytic prescription for constructing hot homogeneous disks in equilibrium. They all have the same surface density σ and gravitational potential Φ as the cold disk in Sec. III A, but differ in the amount of random motion. In these models, the particles have an isotropic velocity distribution in a rotating frame that moves with angular velocity Ω:

$$v \cos \chi = v_\phi - \Omega r, \tag{31}$$

$$v \sin \chi = v_r. \tag{32}$$

Here v is the magnitude of the isotropic velocity in the rotating frame and χ is a random angle about the particle position in the disk plane. The distribution of particle velocities is given by

$$f(v) v dv = 2\pi K \left[v_{\max}^2 - v^2 \right]^{-1/2} v dv. \tag{33}$$

Here

$$v_{\max}^2 = (\Omega_0^2 - \Omega^2)(R_0^2 - r^2), \tag{34}$$

$$\Omega_0 = \frac{h_0}{R_0^2}, \tag{35}$$

and K is a normalization constant. Models in this family are parametrized by the ratio Ω/Ω_0. Cold disks have $\Omega = \Omega_0$. Hot disks with $\Omega/\Omega_0 < 0.816$ are stable against ring formation.

C. Relativistic disk

Here we construct a relativistic generalization of the cold homogeneous Newtonian disk described in Sec. III A. This is useful for studying the dynamical behavior of disks in the strong field region, where almost nothing is known.

Consider a disk of particles in circular equilibrium. The Hamiltonian equation [Ref. [6] Eq. (A6)] reduces to

$$\nabla^2 \psi = -2\pi \frac{\rho^*}{\psi}, \tag{36}$$

where we have temporarily restored a factor of 8π to the right-hand side. We can obtain an analytic solution if we first cast Eq. (36) into Poisson's equation by setting $\rho^*/\psi = 2\rho_N$, obtaining

$$\nabla^2 \psi = -4\pi \rho_N, \tag{37}$$

and then equating ρ_N to the homogeneous Newtonian density profile for an oblate spheroid in the pancake limit [12]. We then find

$$\psi = 1 - \Phi_N, \tag{38}$$

where Φ_N is the Newtonian potential for a flattened spheroid [12]. In the disk interior, this yields

$$\Phi_N = -\frac{3\pi M_N}{4R_0} \left(1 - \frac{1}{2} \frac{r^2}{R_0^2} \right) \quad \text{(interior)}. \tag{39}$$

The total mass of the disk M is related to the Newtonian mass M_N appearing in Φ_N by

$$M = 2M_N. \tag{40}$$

Comparing Eqs. (36) and (37) we find that the surface density Eq. (9) is given by

$$\sigma = 2\psi \sigma_N, \tag{41}$$

where σ_N is the corresponding Newtonian density given by Eq. (19).

The angular motion of a particle in an equilibrium disk is determined by setting $du_r/dt = u_r = 0$ and using Eqs. (A8) and (A13) of Ref. [6]. The result is

$$u_\phi^2 = \frac{(\alpha_{,r}/\alpha) B^2 r^2}{B_{,r}/B - \alpha_{,r}/\alpha + 1/r} \qquad \text{(equilibrium)}, \tag{42}$$

where $B = \psi^2$ is given by Eqs. (38) and (39). The lapse α is found from the maximal slicing ($K_i^i = \partial_t K_i^i = 0$) condition, Eq. (A7) of Ref. [6] specialized to equilibrium, for which $\eta = 0 = \hat{K}_j^i$. The source term Σ appearing in the jump condition for the lapse equation is given by

$$\Sigma = \sigma \frac{u_\phi^2}{B^2 r^2 + u_\phi^2}, \tag{43}$$

where we have used Eq. (A16) of Ref. [6]. Because α and u_ϕ^2 are interdependent, it is necessary to iterate the

lapse equation and Eq. (42). As an initial guess we use $\alpha \simeq 1 + \Phi_N^{(\text{exterior})}$.

The rest-mass surface density σ_0 defined in Eq. (13) is given by

$$\sigma_0 = \frac{2\sigma_N \psi}{(1 + u_\phi^2/B^2 r^2)^{1/2}} \tag{44}$$

from which the total rest mass can be computed using Eq. (12).

We can obtain a solution to the initial value equations for a *nonequilibrium* disk at a moment of time symmetry when the particles are moving at a fraction ξ of their equilibrium velocity:

$$u_\phi = \xi u_\phi^{(\text{equil})}. \tag{45}$$

The other equations remain unchanged. In the Newtonian limit, this solution goes over to the cold oscillating disk of Sec. III A.

An interesting nonequilibrium solution is the one in which $\xi = 0$. This corresponds to the collapse of a homogeneous disk in which all the particles are at rest initially. This is the pancake analogue of Oppenheimer-Snyder collapse of a homogeneous sphere. In the disk case, however, the solution is radiative and is not known analytically. In this case the total mass and rest mass are related by

$$M = \frac{2M_0}{1 + (1 + 6\pi M_0/5R_0)^{1/2}} \tag{46}$$

(see Ref. [12]).

IV. NUMERICAL RESULTS

In this section, we give examples of evolutions computed with our fully relativistic particle disk plus gravity code. Convergence and other tests of the basic code have been reported on in other papers [5–7]. For realistic simulation grids, the convergence properties of the code with the new disk source boundary conditions were consistent with earlier results.

In Table I we summarize the cases discussed in the text. When possible, we show gravitational waveforms and also make contact with analytic results. The waveforms are extracted with the standard gauge invariant extraction method of Abrahams and Evans [13]. The waveforms are extracted at a fixed coordinate radius and displayed as a function of coordinate time. (Our radial coordinate is equivalent to the isotropic Schwarzschild coordinate for spherically symmetric spacetimes.) In certain cases when it was necessary to extract the waveforms at small radii, $r \simeq 10$ M, we tested the procedure by making corrections for the Schwarzschild background. These corrections were of the same order as the inconsistencies in the waveforms extracted at different radii: 10–20%. In Sec. IV B we discuss further the sources of error in the extracted waveforms. We also monitor quasilocal mass indicators; for the runs shown here the total mass is numerically preserved to within about 3%.

A. Oscillating cold Newtonian disk

As a check on our code, one would first like to simulate the collapse of the oscillating homogeneous disk described in Sec. III A. Unfortunately, such a cold configuration is unstable to ring formation. This is the familiar result for cold equilibrium disks with $\Omega = \Omega_0$ and $\xi = 1$ discussed above; we find numerically that it also holds for cold oscillating disks. We can still employ this analytic model to check the field solver in our code provided we supply the unperturbed source function σ analytically as a function of time. We then allow the code to solve the field equations and thereby determine the gravitational radiation numerically from the metric and extrinsic curvature.

Here we give results from a typical evolution of a homogeneous disk with $R_0/M_0 = 30$ and velocity cutdown factor $\xi = 0.9$. This choice of radius is sufficiently large that the system remains essentially Newtonian throughout its evolution. We place the outer boundary at $r_{\max}/M_0 = 500$ and use a mesh with 30 radial zones inside the matter, 220 outside, and 16 angular zones in the upper hemisphere. In Fig. 1 we compare the gravitational waveform extracted at an arbitrary fixed exterior radius of 42 M using a gauge-invariant technique [13], with the analytic prediction Eq. (30). After an initial transient, the waveforms coincide very closely. The slight noise in the extracted waveform arises from interpolation error when the analytic source is mapped onto the numerical grid.

The excellent agreement between the analytic and numerical results here gives confidence in the reliability of the numerical implementation of the jump conditions and the solution of the field equations.

B. Oscillating Kalnajs disk

To test the particle simulation aspects of our code, we set up stable equilibrium Kalnajs disks as described in Sec. III B. Our code successfully holds these in equilib-

TABLE I. Disk evolution cases.

Case	R_0/M	Ω/Ω_0	ξ	Fate
Oscillating cold Newtonian (analytic source)	30.0	1.0	0.9	Oscillates
Oscillating Kalnajs	20.0	0.8	0.9	Oscillates
Cold relativistic equilibrium	8.0	1.0	0.99	Rings
Hot relativistic near-equilibrium	10.0	0.85	1.0	Collapses and virializes
Cold relativistic	1.5	1.0	0.0	collapses to black hole

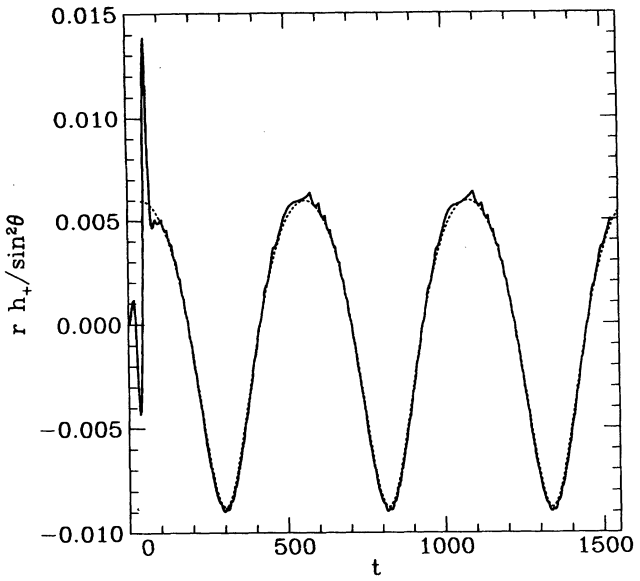

FIG. 1. Gravitational waveform from a cold oscillating disk with an analytic Newtonian matter source. The numerically generated and propagated gravitational waveform (solid line), extracted at a radius of 41 m, is compared with the analytic prediction, Eq. (30) (dotted line). The disk has an equilibrium radius $R_0/M = 30$ and a velocity cutdown $\xi = 0.90$. The wave amplitude h_+ is dimensionless while r and t are in units of M.

rium for several rotation periods.

We next study the production of gravitational radiation from the oscillation of a hot nonequilibrium disk. We set up a Kalnajs disk with $R_0/M_0 = 20$ and velocity dispersion $\Omega/\Omega_0 = 0.8$. We then induce collapse by reducing all particle velocity components by a cutdown factor $\xi = 0.9$. This run employed 200 radial by 32 angular zones and 12 000 particles. Frames from the evolution are shown in Fig. 2. Although some of the collisionless matter from the hot disk escapes, most of the particles stay together and oscillate homologously around the equilibrium radius. In Fig. 3 we compare the extracted quadrupole waveform with h_+ computed numerically from the particle positions and velocities according to the quadrupole formula Eq. (28) with

$$I_{zz} = -\frac{1}{3}\sum_j m r_j^2. \tag{47}$$

As this disk is nearly Newtonian, higher multipoles are expected to contribute negligibly to h_+. The good agreement over several oscillations in Fig. 3 tests many facets of the mean-field particle simulation scheme, including the field and particle integrators, the particle and grid sampling, and the source binning algorithm. Waveforms extracted at different radii agree at the 15% level at this grid resolution. Our experiments indicate that most of this difference, and the difference from the quadrupole calculation, arises from instantaneously propagated errors in solutions of the constraint equations. To remove near-zone and gauge effects, the wave extraction method requires delicate cancellations between different multipole moments. Counter streaming in the particle source can cause inaccuracies: the particle properties vary rapidly over very small spatial distances. This leads to errors in the computed matter source terms whose effects are propagated instantaneously in the parts of the gravitational field computed from the elliptic constraint equations. Parts of the gravitational field that are determined by the hyperbolic evolution equations do not respond to fluctuations in the source instantaeously.

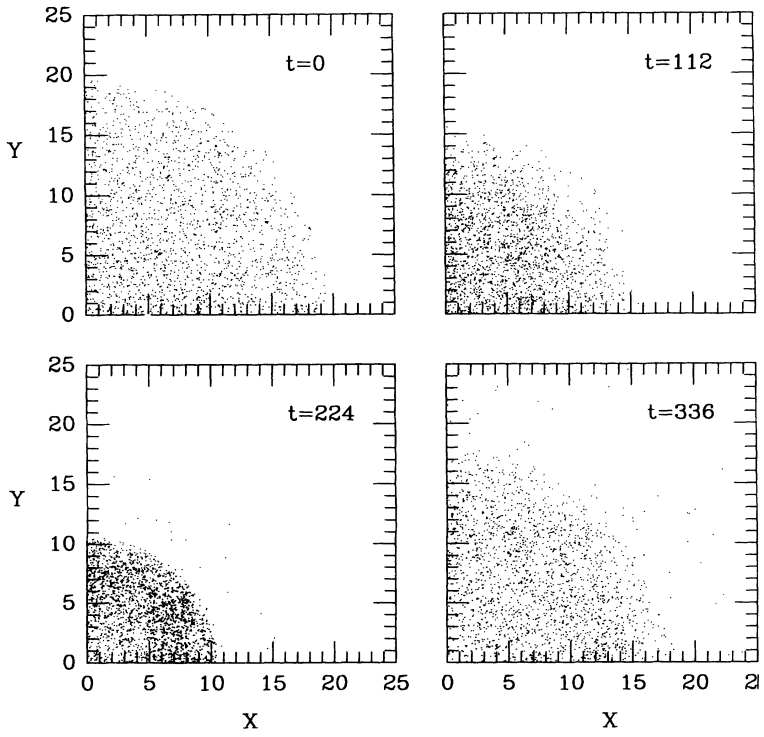

FIG. 2. Snapshots of the particle positions for the evolution of an oscillating Kalnajs disk. The initial radius is $R_0/M = 20.0$, velocity cutdown $\xi = 0.9$, and velocity dispersion parameter $\Omega/\Omega_0 = 0.8$. Particle coordinates and time are in units of M.

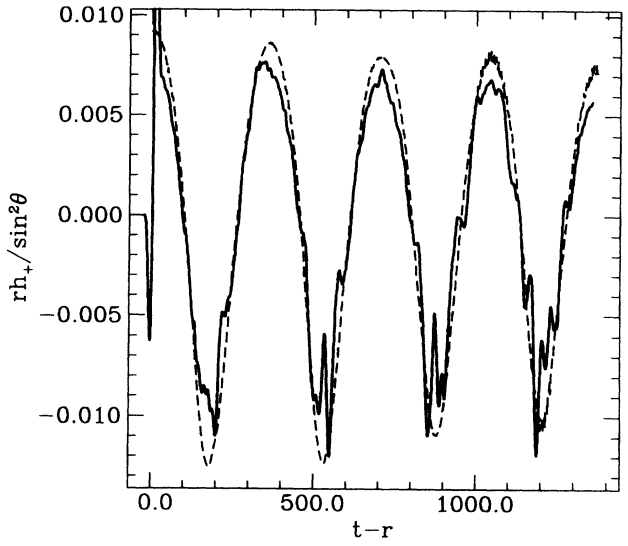

FIG. 3. Gravitational waveform from the oscillating Kalnajs disk shown in Fig. 2. The quadrupole waveform extracted at a radius of $r/M = 21$ (solid line) is compared with the quadrupole formula result, Eq. (28) (dashed line).

This contrasting behavior leads to errors in the extracted waveforms because extraction relies on delicate cancellations of the near-zone field components. However, when smoothed out, the waveforms extracted at different radii agree within the accuracy stated above.

C. Cold equilibrium relativistic disk

Here we consider equilibrium disks constructed according to the prescription of Sec. III C. The question we wish to answer is whether this disk is unstable to rings as in the Newtonian theory when the source and gravitational field are evolved consistently. In Fig. 4 we show a relativistic disk with $R_0/M = 8$. Before the evolution progresses very far, ring formation begins and by $t = 30M$ is completely dominant. Less relativistic configurations behave similarly. This calculation was carried out with 300 radial by 16 angular zones and 12 000 particles, but runs with as many as 48 000 particles did not not slow down the ring formation.

D. Hot relativistic disk

As discussed before, ring formation is suppressed by the addition of sufficient random particle motion. Unfortunately, only small values of velocity dispersion can be used without dissipating the outer region of the disk. Here we consider the evolution of a relativistic disk with $R_0/M = 10$, and velocity dispersion parameter $\Omega/\Omega_0 = 0.85$ and $\xi = 1.0$. Because of its compactness, this near-equilibrium relativistic Kalnajs disk is unstable to collapse. As shown in Fig. 5 the disk initially collapses and then oscillates about a new equilibrium of about $R_0/M = 8.0$. At late times it virializes to a static equilibrium state.

In Fig. 6 the gravitational waveform extracted at $r/M = 12.0$ is compared with the quadrupole formula result. As discussed above, we have evidence that the stochasticity of the particle source is responsible for the short-time scale discrepancies between the waveforms. This calculation used a 200 radial by 16 angular zones and 12 000 particles. Improving the accuracy requires higher grid resolution and more particles; unfortunately

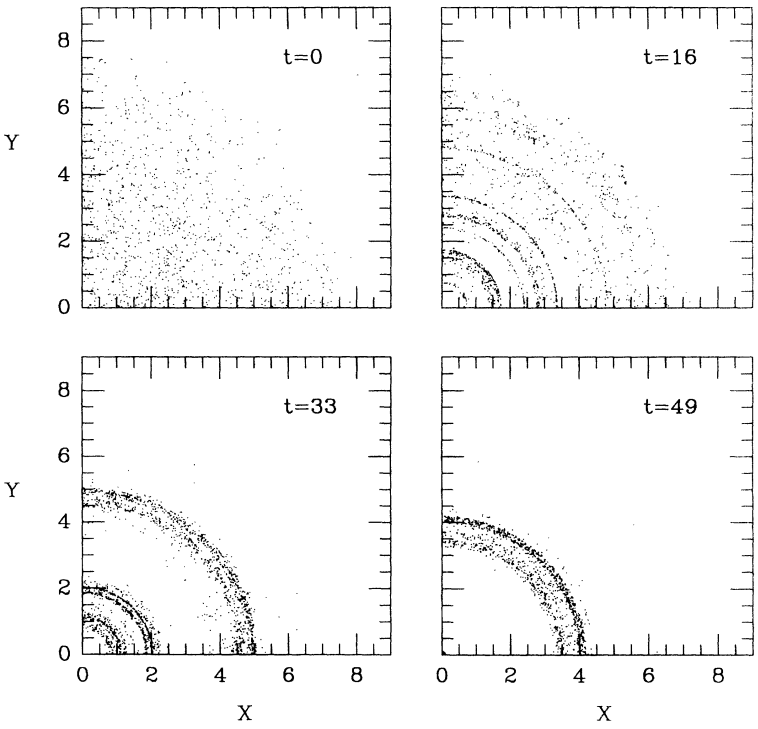

FIG. 4. Snapshots of the particle positions for the evolution of a cold, equilibrium relativistic disk. The initial disk radius is $R_0/M = 8.0$. The rapid growth of concentric rings is apparent.

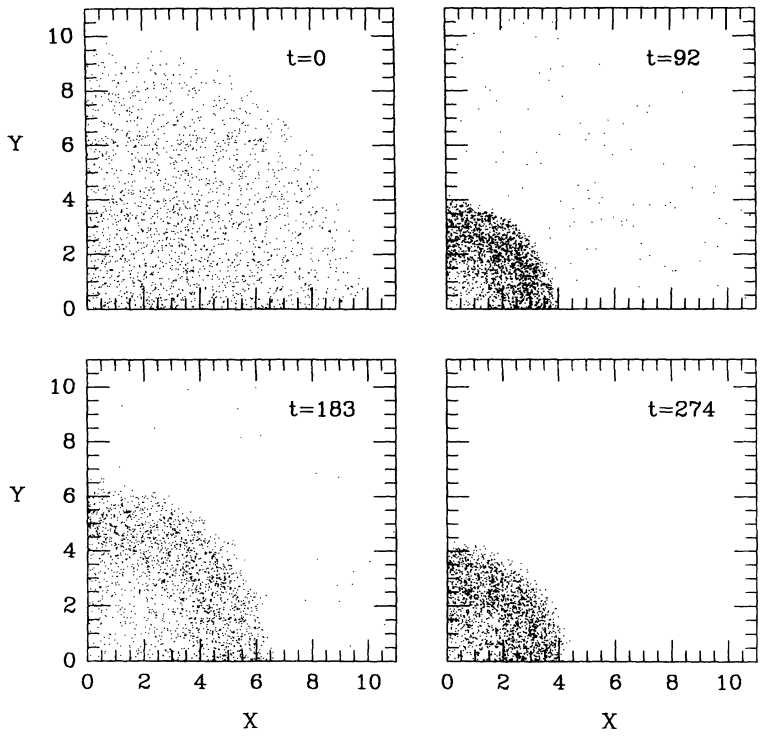

FIG. 5. Snapshots of the particle positions for the evolution of a hot, near-equilbrium relativistic disk. The initial disk radius is $R_0/M = 10.0$ and the velocity dispersion parameter $\Omega/\Omega_0 = 0.85$. Following collapse, the disk settles down to a new equilbrium state.

the noise in the waveform is a $\sqrt{N}$ effect so increasing the number of particles quickly becomes computationally prohibitive.

E. Cold disk collapse

Finally, we consider the collapse of a cold homogeneous disk, the disk analogue of Oppenheimer-Snyder collapse in spherical symmetry. Initially, all particle velocities are equal to zero ($\xi = 0$). We consider a very relativistic case with $R_0/M = 1.5$. (Recall that in isotropic coordinates a Schwarzschild black hole has a radius $R_0/M = 0.5$.) With such a compact disk, the collapse is quick enough that an apparent horizon appears before the ring instability becomes significant. In Fig. 7 we show results from an evolution carried out with 300 radial by 16 angular zones and 24 000 particles. The apparent horizon appears at a time of about 4.0 M and ring formation is just discernible at the disk center at this time.

In order to prolong the numerical evolution after the black hole forms and counteract the effect of "throat stretching" that occurs in our maximal (and other singularity avoiding) time-slicing conditions, we have implemented a moving mesh algorithm that moves the inner radial grid zone to track the growth of the conformal factor ψ. With this method, we are able to evolve the black hole and preserve constancy of out quasilocal mass measures (the Brill and ADM masses) to a few percent for around 15 M after hole formation. Evolution beyond this time is prevented by the numerical difficulties in integrating the particle geodesics on the extremely stretched mesh.

This time is sufficient, however, to see the pulse of radiation from collapse and, perhaps, the first half wavelength of a quasi-normal-mode oscillation. In Fig. 8 we show an estimate of the asymptotic quadrupole waveform extracted at $r/M = 8.0$. After an initial peak representing radiation in the initial data we see an oscillating signal with total wavelength of approximately 16 M, comparable with that of the most slowly damped $\ell = 2$ quasinormal mode oscillation which has $\lambda = 16.8$ M. The energy radiated is less than 0.1% in the quadrupole mode, and we estimate that it is less than 0.01% in higher ℓ-

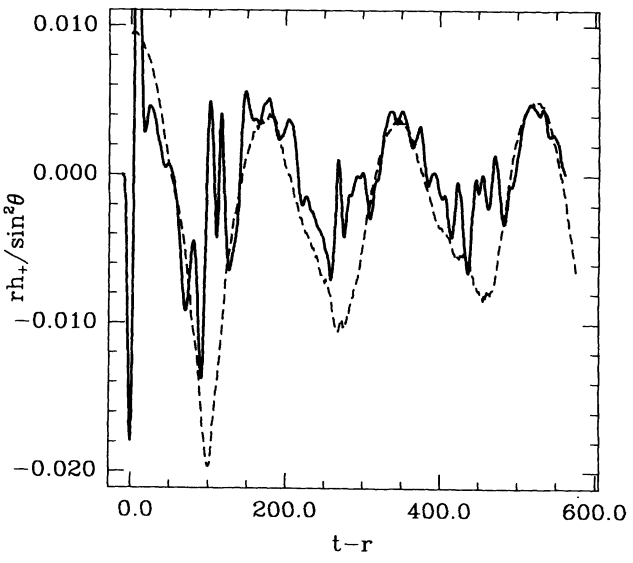

FIG. 6. Waveform from the hot relativistic disk shown in Fig. 5. Wave amplitudes are labeled as in Fig. 3.

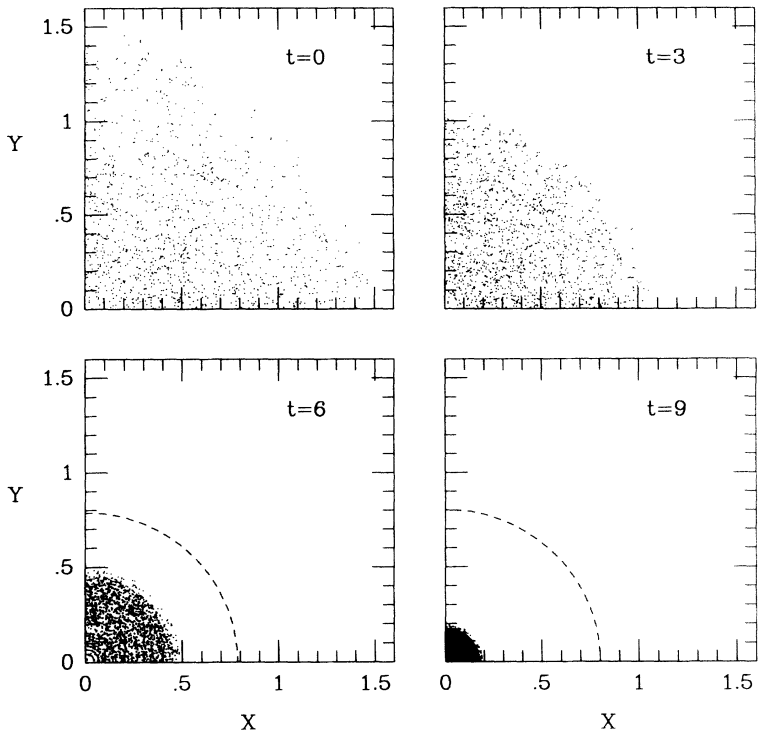

FIG. 7. Snapshots of the particle positions for the collapse of a cold relativistic disk. Initially the radius is $R_0/M = 1.5$ and the particles are all at rest. The apparent horizon (dashed line) first appears at $t \simeq 4.0$ M.

modes. In a future paper [14] we study the waves from this case with a somewhat different method.

We monitor the area of the apparent horizon and its polar and equatorial circumferences (see Ref. [6] for definitions). As shown in Fig. 9, the normalized apparent horizon area $\mathcal{A}/16\pi M^2$ has a value of 0.95 when it first forms, and asymptotes towards the Schwarzschild value of 1.0 before the calculation terminates. The black hole is initially oblate when the apparent horizon forms. The normalized proper circumferences oscillate around their Schwarzschild values $\mathcal{C}_{eq}/4\pi M = \mathcal{C}_p/4\pi M = 1.0$ as the black hole radiates off its initial asphericity. This oscil-

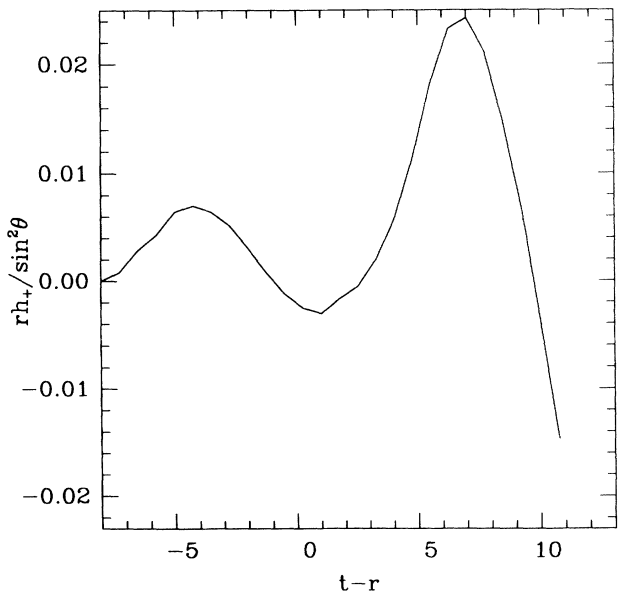

FIG. 8. Gravitational waveform from the disk collapse shown in Fig. 7. The quadrupole waveform extracted at $r/M = 8.0$ is shown as a function of retarded time.

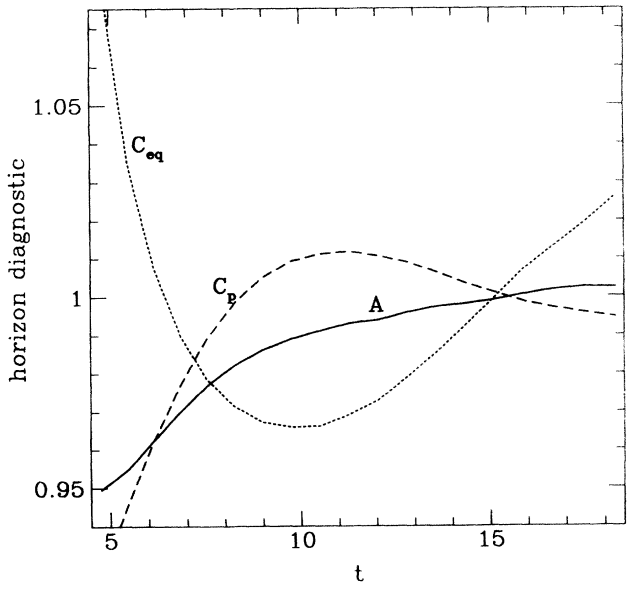

FIG. 9. Horizon diagnostics for the black hole formation shown in Fig. 7. The proper equatorial circumference, polar circumference, and area of the apparent horizon normalized to their Schwarzschild values $\mathcal{C}_{eq}/4\pi M$, $\mathcal{C}_p/4\pi M$ and, $\mathcal{A}/16\pi M^2$ are plotted as functions of time in units of M.

lation period again is comparable with that of the most slowly damped $\ell = 2$ quasinormal mode.

V. CONCLUSIONS

We have presented here preliminary results from a new relativistic mean-field, particle-simulation code that can evolve disks of collisionless matter and compute the emitted gravitational radiation. The disk analogue to the Oppenheimer-Snyder solution, cold homogeneous disk collapse, is an interesting benchmark for numerical relativity codes as it is one of the simplest scenarios that encounters the two most computationally challenging features of relativistic collapse: black hole formation and evolution, and gravitational wave production and propagation. The hydrodynamical formulation of this problem, provided in Sec. II C, should permit implementation of disk collapse in codes without collisionless matter sources.

Failure to complete the computation of the full radiation data in the case of disk collapse to a black hole reflects the fundamental problem in numerical relativity. Specifically, no general algorithm is currently known that can integrate Einstein's equations for long enough after a black hole forms to compute the full gravitational waveform. It may be possible that this problem can be solved with suitable apparent horizon boundary conditions, "cutting out" the black hole (see e.g., Ref [15]). We expect disk collapse to be a useful proving ground for developing apparent-horizon boundary conditions and other black hole evolution techniques in an axisymmetric context.

ACKNOWLEDGMENTS

This work was supported by National Science Foundation Grant No. AST 91-19475 and No. PHY 90-07834 and by Grand Challenge Grant No. NSF PHY 93-18152/ ASC 93-18152 (ARPA supplemented). Computations were performed at the Cornell Center for Theory and Simulation in Science and Engineering, which is supported in part by the National Science Foundation, IBM Corporation, New York State, and the Cornell Research Institute.

[1] See, e.g., C. W. Misner, K. S. Thorne, and J. A. Wheeler, *Gravitation* (Freeeman, San Francisco, 1973), Sec. 32.

[2] S. L. Shapiro and S. A. Teukolsky, Phys. Rev. D **49**, 1886 (1994).

[3] See, e.g., J. Binney and S. Tremaine, *Galactic Dynamics* (Princeton University, Princeton, NJ, 1987), Sec. 5.3.

[4] A. J. Kalnajs, Astrophys. J. **175**, 63 (1972).

[5] S. L. Shapiro and S. A. Teukolsky, Phys. Rev. Lett. **66**, 994 (1991); S. L. Shapiro and S. A. Teukolsky, Am. Sci. **79**, 330 (1991).

[6] S. L. Shapiro and S. A. Teukolsky, Phys. Rev. D **45**, 2739 (1992).

[7] A. M. Abrahams, G. B. Cook, S. L. Shapiro, and S. A. Teukolsky, Phys. Rev. D **49**, 5153 (1994).

[8] R. Arnowitt, S. Deser, and C. W. Misner, in *Gravitation: An Introduction to Current Research*, edited by L. Witten (Wiley, New York, 1962), p. 227.

[9] Note that the source terms appearing in the Appendix of Ref. [6] and used here are related to the components of $T_{\mu\nu}$ by a factor $8\pi A^2 B$. Hence, $\rho^* = 8\pi A^2 B T_{\mu\nu} n^\mu n^\nu$, etc.

[10] S. L. Shapiro and S. A. Teukolsky, Astrophys. J. **235**, 199 (1980).

[11] S. L. Shapiro and S. A. Teukolsky, Astrophys. J. **318**, 542 (1987).

[12] T. Nakamura, S. L. Shapiro, and S. A. Teukolsky, Phys. Rev. D **38**, 2972 (1988).

[13] A. M. Abrahams and C. R. Evans, Phys. Rev. D **42**, 2585 (1990).

[14] A. M. Abrahams, S. L. Shapiro, and S. A. Teukolsky (in preparation).

[15] E. Seidel and W.-M. Suen, Phys. Rev. Lett. **69**, 1845 (1992).